CrossMark

J. Fluid Mech. (2015), *vol.* 770, *pp.* 398–423. © Cambridge University Press 2015
doi:10.1017/jfm.2015.137

Stability of a moving radial liquid sheet: experiments

Manjula Paramati[1], Mahesh S. Tirumkudulu[1,†] and Peter J. Schmid[2]

[1]Department of Chemical Engineering, Indian Institute of Technology Bombay, Powai, Mumbai 400076, India

[2]Department of Mathematics, Imperial College London, London SW7 2AZ, UK

(Received 29 July 2014; revised 13 January 2015; accepted 28 February 2015; first published online 8 April 2015)

A recent theory (Tirumkudulu & Paramati, *Phys. Fluids*, vol. 25, 2013, 102107) for a radially expanding liquid sheet, that accounts for liquid inertia, interfacial tension and thinning of the liquid sheet while ignoring the inertia of the surrounding gas and viscous effects, shows that such a sheet is convectively unstable to small sinuous disturbances at all frequencies and Weber numbers ($We \equiv \rho_l U^2 h/\sigma$). Here, ρ_l and σ are the density and surface tension of the liquid, respectively, U is the speed of the liquid jet, and h is the local sheet thickness. In this study we use a simple non-contact optical technique based on laser-induced fluorescence (LIF) to measure the instantaneous local sheet thickness and displacement of a circular sheet produced by head-on impingement of two laminar jets. When the impingement point is disturbed via acoustic forcing, sinuous waves produced close to the impingement point travel radially outwards. The phase speed of the sinuous wave decreases while the amplitude grows as they propagate radially outwards. Our experimental technique was unable to detect thickness modulations in the presence of forcing, suggesting that the modulations could be smaller than the resolution of our experimental technique. The measured phase speed of the sinuous wave envelope matches with theoretical predictions while there is a qualitative agreement in the case of spatial growth. We show that there is a range of frequencies over which the sheet is unstable due to both aerodynamic interaction and thinning effects, while outside this range, thinning effects dominate. These results imply that a full theory that describes the dynamics of a radially expanding liquid sheet should account for both effects.

Key words: absolute/convective instability, interfacial flows (free surface), thin films

1. Introduction

The process by which bulk liquid is converted into fine droplets using external forces is known as atomization. Atomization plays an important role in many industrial processes such as combustion of liquid fuels in rocket engines, spray painting, encapsulation of biomedical materials, powder metallurgy, removal of toxic materials, and in many other chemical processes (Dombrowski, Hasson & Ward 1960; Weihs 1978). Since the goal of any atomization process is to obtain a desired drop size distribution, it is important to understand the physical processes involved

† Email address for correspondence: mahesh@che.iitb.ac.in

https://doi.org/10.1017/jfm.2015.137 Published online by Cambridge University Press

in the break-up of the liquid. In many spray nozzles, the liquid is forced through an orifice leading to the formation of liquid jets that break up into droplets. In others, a liquid sheet forms first, which subsequently breaks up into ligaments and drops. In all these cases, linear instability theories are used to predict the wavelength of the most unstable disturbance wave, which in turn provides an estimate of the drop size distribution. The instability theories also form the basis for sophisticated atomization models designed to predict the drop size distribution in spray systems (Ashgriz 2011). Consequently, it is important to understand the physics underlying the break-up process, not only to predict the drop-size distribution, but also to design nozzles that achieve the desired distribution.

Impinging jet injectors, the focus of this study, are the most common configuration for atomization in high-density combustors due to their relative simplicity of fabrication, as well as their atomization and mixing characteristics (Shen, Mitts & Poulikakos 1997). Much of the early work on the stability of the radial liquid sheet (Huang 1970; Weihs 1978) formed by impingement of liquid jets was an extension of the classical temporal instability analysis of Squire (1953), who studied the instability of a thin inviscid planar liquid sheet of constant thickness moving in a quiescent ambient gas medium. The constant sheet thickness analysis shows that the sheet is unstable to sinuous waves only when the Weber number, calculated with respect to the local thickness (h), $We \equiv (\rho_l U^2 h)/\sigma > 2$ and $\rho_a/\rho_l \neq 0$, where ρ_l and ρ_a are the densities of the liquid and gas phase respectively, σ is the surface tension of the liquid, and U is the speed of the liquid. The theory does not predict instability in the absence of the gas phase. On the experimental side, Huang (1970) performed experiments at ambient conditions with radially expanding liquid sheets produced by head-on impingement of two equal laminar jets. Assuming no energy losses at the point of impingement, so that the fluid speed into the stagnation point is equal to the speed exiting the stagnation point, leads via a simple mass balance to the following thickness variation in the radial direction:

$$h = \frac{d^2}{4r}. \tag{1.1}$$

Here, d is the diameter of the laminar jet and r is the radial distance from the impingement point. For low jet speeds corresponding to $We_d \equiv \rho_l U^2 d/\sigma < 500$, where the Weber number is calculated based on the jet diameter, the surface of the sheet is smooth in the absence of external disturbances and the sheet radius increases linearly with We_d with a near-perfect circular edge. For $500 < We_d < 800$, there is a small deviation from the linear relation. Small disturbances generated at the point of impingement generate capillary waves that propagate radially outwards and converge at the periphery, resulting in a cusp-shaped edge of the liquid sheet. Overall, the sheet is considered to be smooth for $We_d < 800$, and this regime is referred to as the smooth regime. In this regime, the edge of the sheet is set by a balance between liquid inertia that spreads the sheet and surface tension that opposes it. Taylor (1959) showed that such a balance leads to $We = 2$ at the edge of the sheet, which corresponds to a sheet radius of

$$\frac{R}{d} = \frac{We_d}{8}. \tag{1.2}$$

For very high jet speeds corresponding to $We_d > 2000$, the sheet becomes unstable to Kelvin–Helmholtz (KH) instability (Squire 1953), caused by the aerodynamic interaction of the liquid sheet with the surrounding air, and this regime is referred to as the flapping regime. In this regime, the sheet diameter reduces with increasing

https://doi.org/10.1017/jfm.2015.137 Published online by Cambridge University Press

We_d with $We > 2$ at the edge of the sheet. A gradual transition to the flapping regime is observed in the range $800 < We_d < 2000$, and hence this range corresponds to the transition regime. The presence of the three regimes was confirmed by Villermaux & Clanet (2002) for the case of a circular sheet produced by a single laminar jet impinging on an impactor. It was shown that the transition from the smooth to the flapping regime is dependent on the ratio of the density of the surrounding gas to the liquid density,

$$\sqrt{\frac{\rho_a}{\rho_l}}We_{d,c} \approx 40, \tag{1.3}$$

where $We_{d,c}$ is the critical Weber number beyond which the flapping regime starts to set in. For the case of water sheets formed in air at atmospheric pressure, $We_{d,c} \approx 1100$.

On the theoretical side, Lin & Jiang (2003) considered the spatio-temporal stability of the radially expanding liquid sheet and reported the sheet to be stable to both sinuous and varicose disturbances in the absence of the gas phase. The stability of the radial liquid sheets was investigated experimentally by Bremond, Clanet & Villermaux (2007), who used a laminar jet that impinged on a vibrating impact cylinder (impactor) to produce wavy (sinuous) radial liquid sheets at low to moderately high jet speeds, so that the flow ranged from smooth to the transition regime ($We_d \sim 250$–1000). The measured envelope of the sinuous wave for the $We_d = 990$ agreed with the predictions of classical linear stability results, following the Squire analysis, when the predicted growth rates were reduced by a factor of half. Thus it appears that the results based on the classical stability analysis of Squire for large We_d (and therefore for the transition/flapping regime) agree well with the measurements for radial sheets, suggesting that for the regimes tested, the principal source of instability is the aerodynamic force arising from interaction of the liquid sheet with surrounding gas medium. However, despite the result of Taylor (1959), who showed that a steady sinuous disturbance introduced at the point of impingement of a radially expanding sheet increases along the radial direction in the absence of the gas phase and diverges at the sheet edge, none of the above studies have investigated the influence of thinning of liquid sheet on the overall stability of the sheet.

In a previous paper (Tirumkudulu & Paramati 2013), it was shown theoretically that a radially expanding liquid sheet produced by two laminar liquid jets impinging head-on is unstable to sinuous disturbances at all forcing frequencies in the absence of the surrounding gas phase. The stability of an expanding liquid sheet as a function of a characteristic Weber number, $We_H \equiv \rho_l U^2 H/\sigma$, was obtained from the inviscid flow equations that govern the time-dependent evolution of the two liquid interfaces while ignoring the inertia of the surrounding gas phase. Here, H is the characteristic thickness of the liquid sheet at a characteristic radial distance of L, and the two are related by $H = d^2/4L$ for a liquid sheet produced by a head-on impingement of two laminar jets (1.1). (To avoid confusion with symbols used for the radial extent of a liquid sheet, we replace the symbol R, used in the previous paper for characteristic radial distance, with L). The analysis yielded stability equations for sinuous and varicose modes that are decoupled at the lowest order of approximation (Tirumkudulu & Paramati 2013),

$$\frac{\partial \bar{F}_-}{\partial \bar{t}} + \frac{\partial \bar{F}_-}{\partial \bar{r}} = 0, \quad \text{and} \tag{1.4}$$

$$\frac{1}{We_H}\left[\frac{1}{\bar{r}}\frac{\partial}{\partial \bar{r}}\left(\bar{r}\frac{\partial \bar{F}_+}{\partial \bar{r}}\right)\right] = \frac{1}{2\bar{r}}\left(\frac{\partial^2 \bar{F}_+}{\partial \bar{t}^2} + 2\frac{\partial^2 \bar{F}_+}{\partial \bar{r}\partial \bar{t}} + \frac{\partial^2 \bar{F}_+}{\partial \bar{r}^2}\right) - \frac{1}{2\bar{r}^2}\left(\frac{\partial \bar{F}_+}{\partial \bar{r}} + \frac{\partial \bar{F}_+}{\partial \bar{t}}\right). \tag{1.5}$$

https://doi.org/10.1017/jfm.2015.137 Published online by Cambridge University Press

Here, $\bar{F}_-$ and $\bar{F}_+$ are the dimensionless perturbed film thickness (varicose mode) and position of the centreline (sinuous modes), both rendered dimensionless with H, $\bar{r}$ is the dimensionless radial coordinate which has been rendered dimensionless with L, and $\bar{t} \equiv tU/L$ is the dimensionless time. We seek solutions of the form

$$\bar{F}_+ = S(\bar{r})\mathrm{e}^{\mathrm{i}\bar{\omega}\bar{t}}, \tag{1.6}$$

$$\bar{F}_- = Q(\bar{r})\mathrm{e}^{\mathrm{i}\bar{\omega}\bar{t}}, \tag{1.7}$$

where $\bar{\omega} \equiv \omega L/U$ is the dimensionless frequency. The varicose mode is a neutrally stable travelling wave, while the sinuous mode is governed by the following equation (Tirumkudulu & Paramati 2013):

$$\left(\frac{1}{2} - \frac{\bar{r}}{We_H}\right)\frac{\mathrm{d}^2 S}{\mathrm{d}\bar{r}^2} = \left(-\mathrm{i}\bar{\omega} + \frac{1}{2\bar{r}} + \frac{1}{We_H}\right)\frac{\mathrm{d}S}{\mathrm{d}\bar{r}} + \left(\frac{\bar{\omega}^2}{2} + \mathrm{i}\frac{\bar{\omega}}{2\bar{r}}\right)S. \tag{1.8}$$

A small sinuous displacement introduced near the point of impingement ($S|_{\bar{r}=1} = S_0 \ll 1$) grows as it is convected downstream, suggesting that the sheet is unstable at all We_H in the absence of the gas phase. Two different wave trains, differing in wave speeds, are generated at the point of impingement and propagate radially outwards. The phase velocity of one train decreases with radial distance while that of the other increases. It was shown that at $\bar{r} = We_H/2$, which corresponds to $We = 2$, the phase speed of the slower wave train decreases to zero while the overall amplitude of the sinuous disturbance diverges, thereby setting the extent of the sheet. These results thus extend the earlier result of Taylor (1959), who showed that a steady disturbance (with zero frequency) introduced at the point of impingement will grow and diverge at the sheet edge.

The objective of this work is to test the predictions of the aforementioned theory (Tirumkudulu & Paramati 2013), which accounts for thinning effects by measuring the evolution of sinuous and varicose waves at varying forcing frequencies and for $We_d = 540$ and 990, pertaining to the smooth and transition regimes, respectively, where the influence of the surrounding gas phase is either negligible or is not dominant at all radial locations of the radial sheet. It will be shown that the predictions of the theory capture the main aspects of the sinuous wave growth far from the impingement point without the need for any fitting/adjustable parameters. It is further shown that, irrespective of the value of We_d, there is always a range of forcing frequencies outside which the thinning effects will dominate over aerodynamic interactions at all radial locations of the liquid sheet. We also compare the predictions of the theory with experiments reported by Bremond *et al.* (2007) for $We_d = 850$ and 990, again pertaining to the transition regime, and found similar agreement. These results indicate that all previous theories (Huang 1970; Weihs 1978; Villermaux & Clanet 2002; Lin & Jiang 2003; Bremond *et al.* 2007) dealing with the radially expanding liquid sheets have missed an important aspect of the problem, namely, a thinning sheet is inherently unstable to sinuous waves and does not necessarily require interaction with the surrounding gas medium to make it unstable. Since the final droplet size distribution is influenced by the wavelength of the most unstable mode, it is important to account for the effects of both aerodynamic interactions and thinning in order to correctly predict the final drop-size distribution.

To test the predictions, experimental determination of the varicose and the sinuous mode of the disturbance necessitates measurement of both the instantaneous local sheet thickness and the displacement of the liquid sheet at varying frequencies. While

https://doi.org/10.1017/jfm.2015.137 Published online by Cambridge University Press

past investigations have measured the sheet thickness in the absence of forcing and sheet displacements in the presence of forcing, very few studies have attempted to measure both simultaneously. This is because reliable measurement of sheet thickness is a difficult task owing to its small thickness. The reported measurement techniques of sheet thickness can be broadly categorized into two groups: contact and non-contact methods. Among the contact methods, Taylor (1959) was the first to measure the sheet thickness by inserting a flow measuring device to measure the volume of a liquid passing through a small section of the sheet. The flow measuring device is made up of a narrow slit attached to a tapering box. The thickness of the liquid sheet at a particular location was then determined from the measured output and the known slit dimensions, assuming the velocity of the sheet is constant and equal to the jet velocity. While this is a simple method, the insertion of the flow-measuring device disturbs the sheet. An alternative technique among the contact methods is the conductivity technique (Brown, Andruessi & Zanelli 1978). This method uses two parallel conducting wires that are in contact with water, and the amount of current that flows between them is proportional to the local thickness of the liquid sheet. The drawbacks of this method are that (i) it can be applied only for conducting liquids, and (ii) contact with the liquid sheet disturbs the flow.

The non-contact methods are mainly optical in nature, involving interference and/or fluorescence. Among these, the interference technique is the most commonly used for the measurement of thickness variations in a liquid sheet (Dombrowski *et al.* 1960; Matsumoto & Takashima 1971; Choo & Kang 2001; Villermaux & Clanet 2002; Bremond *et al.* 2007), including soap films (Liang & Chan 1997). In this case, interference fringes represent contours of constant thickness so that the profiles of the film thickness can be constructed from the distance between fringes. This requires that the distance between the fringes and the angle of incidence of the laser beam with respect to the liquid sheet are known to sufficiently high precision. However, in regions where the film thickness varies rapidly, e.g. close to the impingement point, the fringes are closely spaced and can be difficult to resolve. Further, this technique is difficult to apply due to a changing angle of incidence when the liquid sheet oscillates, such as in the flapping regime or when the sheet is exposed to external pressure fluctuations. To overcome these constraints, Wakimoto & Azuma (2004) captured the cross-section of a liquid sheet using a laser-induced fluorescence (LIF) technique by passing a laser sheet at an acute angle to the plane of the liquid sheet which contained a fluorescent dye. The camera was placed at an acute angle to the liquid sheet on the opposite side so that the cross-section of the liquid sheet could be imaged. A calibration was performed so that the distance between the upper and lower boundaries of the fluorescent image yielded the true film thickness. A different approach to extracting thickness information using the LIF method has been applied to liquid films flowing over a solid substrate or confined between transparent solid substrates (Alekseenko *et al.* 2009). Here, a non-linear Beer–Lambert law relating the incident light intensity, emission light intensity, film thickness, fluorescent dye concentration and extinction coefficient was used to determine the local variations in the film thickness. A more advanced technique proposed by Hidrovo & Douglas (2001) employs a dual emission LIF technique for the measurement of liquid-film thickness, where the fluid contains two dyes such that the emission spectrum of one dye overlaps the absorption spectrum of another dye. The ratio of the emission intensity of the two dyes obtained from the Beer–Lambert law for the case of very thin liquid films is independent of the intensity of the incident light, and becomes a function of thickness alone.

https://doi.org/10.1017/jfm.2015.137 Published online by Cambridge University Press

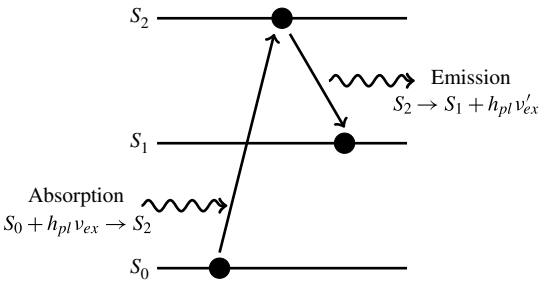


FIGURE 1. Absorption and emission of a photon by a fluorescent molecule due to the collision of a dye molecule with surrounding molecules.

In this paper, we employ a simple planar LIF technique similar to that of Alekseenko *et al.* (2009) to measure the instantaneous local thickness of a thin moving liquid sheet. This technique captures not only the thickness profiles of an undulating liquid sheet but also the centreline displacement of the wavy liquid sheet responding to external disturbances. Thus, knowledge of the thickness variation along with the lateral displacement of the liquid sheet can be used to characterize the wave motion in terms of wave amplitude, growth rates and phase velocities of both sinuous and varicose modes. The measured thickness profiles for the smooth liquid sheet ($We_d \leqslant 540$) and in the absence of external disturbances shows the expected $1/r$ dependence, and is in good agreement with theoretical predictions for a wide range of We_d. In the presence of external forcing, the sheet thickness is indistinguishable from that measured in its absence, suggesting that the varicose wave amplitudes fall below the resolution of our experimental technique (± 0.5 μm being the standard deviation). On the other hand, the measured sinuous phase velocities and growth rates vary with radial distance and are compared with the predictions of Tirumkudulu & Paramati (2013). The remainder of the paper is organized into three parts: the first dealing with the experimental methodology for measuring the sheet thickness, the second part presenting the results of our experiments and comparison with theory, and the third part offering comments on the implications of this study.

2. Experimental methodology

2.1. *Basic principle of the LIF technique*

LIF is based on the principle that electrons of fluorescent molecules can be moved from a ground state (S_0) to an electronically excited state (S_2) by incident photons of energy $h_{pl}\nu_{ex}$, as shown schematically in figure 1 (Crimaldi 2008). Here, h_{pl} denotes Planck's constant, and ν_{ex} is the frequency of incident light. The excited molecules relax to an intermediate state (S_1) by emitting a photon excitation light of energy $h_{pl}\nu'_{ex}$ due to collision of the excited molecules with surrounding molecules in the excited state. Owing to energy dissipation during the excited-state life time, the energy of an emitted photon is always lower than the excited energy of the photon (i.e. $\nu'_{ex} < \nu_{ex}$).

The amount of absorbed excitation light by a given volume of fluid containing fluorescent molecules can be expressed by Beer–Lambert's law,

$$I_A = I_0 - I_0 \mathrm{e}^{-\epsilon hc} = I_0(1 - \mathrm{e}^{-\epsilon hc}). \tag{2.1}$$

Here, I_A denotes the absorbed power, I_0 stands for the excitation power, ϵ is the molar extinction coefficient which depends on the wavelength of the incident light,

https://doi.org/10.1017/jfm.2015.137 Published online by Cambridge University Press

h represents the path length through the sample, and c is the concentration of fluorophore species. Accordingly, the amount of emitted fluorescence energy (I_f) is proportional to the absorbed energy (I_A) and the quantum efficiency of the dye (ϕ_{dye}),

$$I_f = I_A\phi_{dye} = I_0\phi_{dye}(1 - \mathrm{e}^{-\epsilon hc}). \tag{2.2}$$

2.2. *Applying LIF to a moving liquid sheet formed by jet impingement*

The schematic diagram of the experimental set-up is shown in figure 2, and is similar to that reported earlier (Mulmule, Tirumkudulu & Ramamurthi 2010). Two identical converging nozzles made up of borosilicate glass with an exit diameter of 1.62 mm and a length of 12 cm are used in the present experiments to obtain liquid sheets over a range of Weber numbers ($We_d = 300$–1000). A three-dimensional traverse is used to position the two nozzles so that the gap between the two nozzles is maintained at approximately 3 mm, and the horizontal axes of the two nozzles are adjusted with rotating stages so that they are accurately aligned. A gear pump is used to pump the liquid from a tank to the nozzles, and the flow through the nozzles is controlled with the help of rotameters. The gear pump delivers smooth and pulseless flow, and consequently does not introduce disturbances into the flow. Experiments were also performed by connecting the piping to a continuous supply of water from overhead tanks situated at a height of around 16 m with respect to the experimental set-up. The results were identical, and therefore most experiments were performed with the pump. Flow through the rotameters is calibrated with the help of a measuring cylinder and the measurement error in flow rate was less than 4 %. Two air vent valves are used to remove air bubbles so as to eliminate disturbances in the flow. The liquid sheet is formed by a head-on impingement of two opposing jets; ejected droplets from the periphery of the sheet are collected in a tray placed below the traverse, and the same is recirculated to the tank. The axial distance between the tip of each nozzle and the point of jet collision was carefully adjusted to obtain a smooth and steady liquid sheet.

The components necessary to carry out the liquid-sheet thickness measurements are the jet impingement set-up as described above, fluorescent dye, an incident laser light sheet and an optical system for the measurement of the fluorescent emission. We chose Rhodamine 6G fluorescent dye for the present work because its physical properties are ideal: absorption (530 nm) and emission (560 nm) spectra are completely separate, the dye is water-soluble and has high quantum efficiency and, furthermore, its excitation wavelength matches the available Argon-Ion laser light source. The fluorescent dye of known concentration is uniformly mixed in water to avoid the formation of any dye aggregates. A thin vertical laser sheet ($\sim$0.1 mm thickness) is generated by passing the laser beam through a cylindrical lens. The vertical laser sheet slices the liquid sheet in a direction perpendicular to the liquid sheet (figure 2). This results in the emission of fluorescent light along a vertical line formed by the intersection of the laser sheet and the liquid sheet. The laser sheet is passed slightly off-centre through the liquid sheet as the piping system and the nozzle arrangement prevent it from passing through the centre of the liquid sheet. The emission from the fluorescent region is captured with a light-sensitive high-speed CCD camera (Pike® F032B model) for varying liquid flow rates. The camera is capable of achieving frame rates up to 1000 f.p.s. at a pixel resolution of 640 $\times$ 50 pixels. The measurement of the liquid-sheet thickness and the position of the centreline of the liquid sheet require two different camera positions. For the former, the camera is placed facing the liquid sheet almost parallel to the laser

https://doi.org/10.1017/jfm.2015.137 Published online by Cambridge University Press

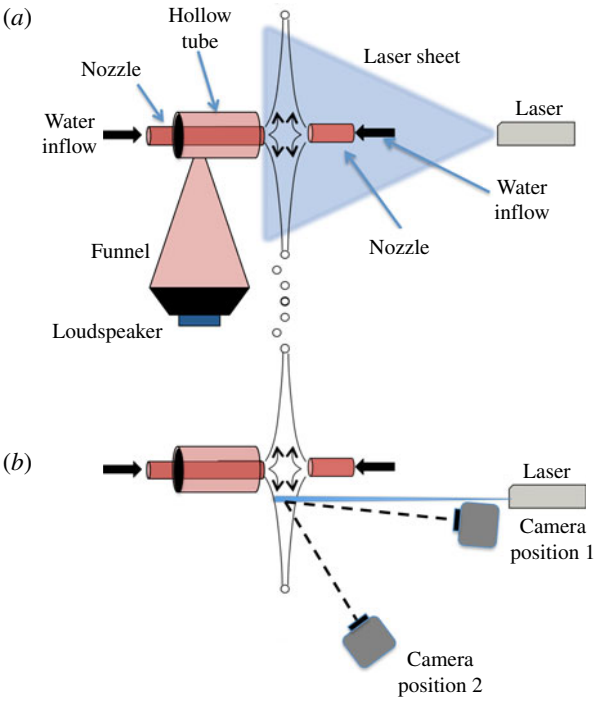


FIGURE 2. (Colour online) Schematic diagram of the experimental set-up. (*a*) Side view including the speaker arrangement for introducing disturbances at the impingement point. (*b*) Top view with the camera positions for measuring the thickness modulation (position 1) and centreline displacement (position 2).

sheet (camera position 1, figure 2*b*) so that the intensity variations due to thickness modulations can be observed clearly. The camera is placed at an acute angle to the liquid-sheet surface (camera position 2, figure 2*b*) for the measurement of the liquid sheet's centreline displacement.

For the conditions of the experiments presented here, the product of the molar extinction coefficient and dye concentration is in the range $c\epsilon = 54$–$62\ \mathrm{cm}^{-1}$ with the value of $\epsilon = 116\,000\ \mathrm{M}^{-1}\ \mathrm{cm}^{-1}$ (Birge 1987). As the thickness of the liquid sheet is very small ($h \ll 1/\epsilon c$), (2.2) can be simplified to obtain the fluorescence emission at any location on the sheet:

$$I_{thin} \approx I_0 \phi_{dye} \epsilon h c. \tag{2.3}$$

The above expression shows that the fluorescence emission is proportional to the incident light intensity, dye characteristics of fluorophore and path length of the liquid film. Once the concentration of the fluorescent species and the solvent is fixed, the only unknown in (2.3) apart from the film thickness is the laser sheet intensity (I_0) along its transmitted path through the liquid sheet. The incident laser sheet intensity varies spatially, which was determined by performing calibration experiments with optically thick films of known thickness ($h \gg 1/\epsilon c$), so that for the conditions of the experiments, (2.2) simplifies to

$$I_{thick} \approx I_0 \phi_{dye}. \tag{2.4}$$

In our experiments, thick films were obtained by using a rectangular cuvette of known dimensions (height 20 cm, width 4 cm, thickness 1 cm) filled with the

https://doi.org/10.1017/jfm.2015.137 Published online by Cambridge University Press

same fluorescent solution as that used for the liquid sheet experiment. The cuvette was placed in the path of the laser sheet at the same location as the liquid sheet. The fluorescence emission from the illuminated vertical section of the cuvette was recorded with all settings of the laser and the camera, such as the laser operating power, camera position, shutter speed and exposure time, kept identical to that for the liquid-sheet experiments. Once I_{thick} is known, (2.3) and (2.4) together give the thickness of the liquid sheet:

$$h = \frac{I_{thin}}{I_{thick} \epsilon c}. \tag{2.5}$$

The fluorescent intensities are obtained by post-processing the captured images in terms of grey levels along the illuminated sections (using ImageJ® and Matlab® software).

2.3. *Liquid-sheet experiments with acoustic forcing close to the jet impingement location*

Acoustic disturbances were introduced close to the jet impingement location resulting in an undulating liquid sheet. This was achieved with a high-sound-intensity speaker (P Audio® C12-500 MB, 50 Hz–2 kHz, programming power of 500 W and sensitivity of 96 dB) connected to a QSC® GX5 (500 W @ 8 Ω) amplifier, which in turn was connected to an Agilent® 33220A signal generator. The latter was tuned to generate signals of varying frequencies and amplitudes. The mouth of the speaker was covered by the diverging end of a conical funnel while the converging end was connected to a hollow tube concentric with one of the water nozzles (figure 2*a*). The quality of the acoustic signals close to the impingement location was checked with the help of a B&K® 2250L sound level meter for different frequencies and sound pressure levels (SPLs). In all cases, the frequency of the dominant peak was identical to that generated by the signal generator. Peaks were also observed at higher harmonics but their intensity was lower by at least 30 dB. As soon as the acoustics are switched on, waves appear close to the impingement location and propagate outwards along the radial direction. It was also ensured that the sound level was uniform around the mouth of the nozzle. This was confirmed by measuring the SPL at different locations around the nozzle.

We also checked whether acoustic forcing causes any significant variation in the diameter of the liquid jet. The jet was imaged at various frequencies and amplitudes, and it was found that there was no perceptible variation in the jet diameter, at least within the camera's resolution (1 pixel = 8 μm), which is less than 1 % of the jet diameter. We also determined whether external acoustic forcing leads to flow rate variations. Polyamide particles were dispersed in water and their motion was imaged inside the nozzle in the presence of acoustic forcing. A laser sheet aligned along the axis of the nozzle and intersecting it along its vertical diameter revealed the motion of the particles via a camera placed transverse to the plane of the sheet. The captured images are processed to track the position of particles with time for each applied frequency, and the velocity of the particles for each radial position was determined as a function of time. There was no perceptible periodic motion of the particles with acoustic forcing within the resolution of the applied technique, with the velocity being the same irrespective of the forcing frequency. These results demonstrate that there is no variation in jet diameter, nor is there any change in the velocity of the fluid in the presence of acoustic forcing. Based on the above tests and the visualization of the displacement of the sheet under fluorescence (to be described later), it is concluded that sinuous disturbances originate at the impingement point and are convected radially outwards.

https://doi.org/10.1017/jfm.2015.137 Published online by Cambridge University Press

Finally, the sheet displacement at any location (along the fluorescent line) is obtained by subtracting the position of the fluorescent line in the presence of acoustics with that in its absence. As figure 2 shows, the camera in position 2 is used to determine the displacement of the sheet centreline. Given that the line of sight (represented by the dashed line) is at an angle of about 10° to the plane of the liquid sheet, the measured displacement will be somewhat less (by $\cos(10°) \sim 0.984$) than the true value. However, the normalized displacement of the sheet centreline obtained by scaling the measured displacement with that measured at the lowest radial location, will be the same irrespective of this angle. We also note that the largest displacements lead to relatively small slopes ∼0.2–0.3 (angle ∼10°–15°). For very large slopes, we expect sections of the fluorescent line to be blocked by parts of the deformed sheet present in the light path between the fluorescent line and the camera. However, this did not happen in any of the experiments, confirming that the deformations were small.

3. Results and discussion

3.1. *Thickness distribution of a smooth liquid sheet in the absence of forcing*

Figures 3(*a*) and 3(*b*) present the emissions from the fluorescent section of liquid sheet for $We_d = 332$ and 478, respectively, which was off-centre by 2.9 cm from the impingement point. The emission images have been rotated by 90°, with the direction of gravity being from left to right. The corresponding extracted thickness distribution along the vertical fluorescent line is given in figures 3(*c*) and 3(*d*), respectively. The solid line in the plots represents the theoretical thickness distribution (1.1). The measurements closely follow the theoretical line for the entire thickness range. The scatter in the experimental data was quantified by calculating the standard deviation about a moving average of the experimental data points. For all cases, the standard deviation was less than 0.5 μm (which sets the resolution of the technique). An important point to note from figure 3(*c,d*) is that the measured thickness profile is nearly identical for the two cases, thereby confirming that the thickness profile is independent of We_d. The maximum thickness along the vertical line for both cases is found to be $h_{max} = 23 \pm 0.5$ μm, which closely matches the theoretical value $h_{max} = 22.5$ μm.

Figure 4 shows the thickness distribution of a smooth liquid sheet ($We_d = 540$) at two different vertical sections off-centre by 2.9 and 5.0 cm from the impingement point. Since the vertical sections are different for the two cases, the profiles are also different. For the profile that is 2.9 cm away from the impingement point, $h_{max} = 23 \pm 0.5$ μm, and that for 5.0 cm, $h_{max} = 13.8 \pm 0.5$ μm, both of which agree rather well with the theoretical maximum-thickness values of 22.5 and 13 μm, respectively. Close inspection of the measured profiles in all cases (including figure 3*c,d*) shows that the sheet thickness in the upper regions of the sheet is slightly larger than that in the lower region of the sheet. This small difference is attributed to the effect of gravity, which slows the liquid as it flows upwards, leading to a marginally larger-than-predicted thickness in the upper regions and *vice versa* for the lower regions of the sheet.

These results suggest that the LIF technique can be successfully employed to measure the thickness distribution of thin moving liquid sheets. Next, the technique is applied to undulating liquid sheets to determine both the thickness modulation and the position of the centreline.

3.2. *Thickness distribution of a liquid sheet with acoustic forcing*

Before discussing the results of the LIF technique, it is instructive to visualize the undulating liquid sheet under normal light conditions. Figure 5(*a–i*) show the response

https://doi.org/10.1017/jfm.2015.137 Published online by Cambridge University Press

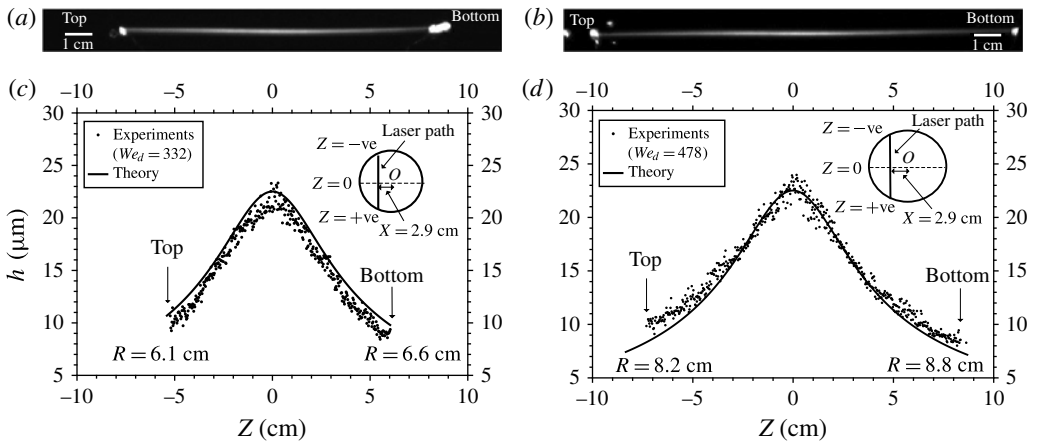


FIGURE 3. (*a*,*b*) Emission from the fluorescent section of the liquid sheet for (*a*) $We_d = 332$ and (*b*) $We_d = 478$. The emission images have been rotated by 90° with the direction of gravity being from left to right. (*c*,*d*) The corresponding extracted thickness distributions. The solid line represents the theoretical thickness distribution (1.1). The insets in (*c*,*d*) include a schematic of the circular sheet along with the position of the intersecting vertical laser sheet. The bright rim region at the sheet edge seen in (*a*,*b*) has been omitted in the plot.

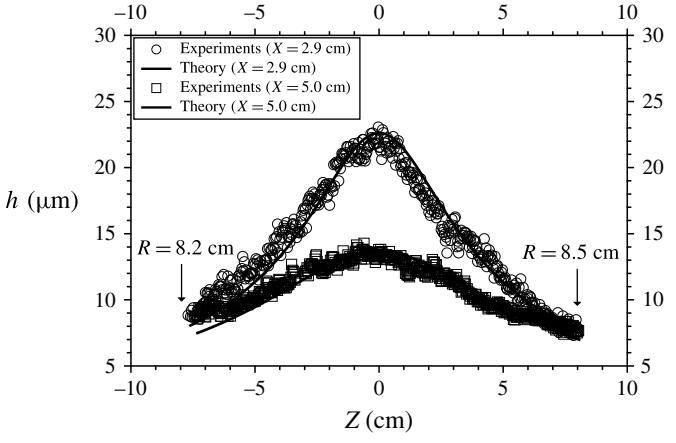


FIGURE 4. Thickness distribution of a liquid sheet for $We_d = 540$ at two different vertical sections that are off-centre by 2.9 cm, and 5.0 cm from the jet impingement point. The solid line represents the theoretical prediction (1.1).

of the liquid sheet at $We_d = 540$ subjected to forcing at a frequency of 90 Hz and an SPL of 85 dB at the impingement point. Figure 5(*a*) shows the smooth liquid sheet just before the acoustics was introduced. After switching on the acoustics, surface ripples appear first near the impingement location, and they travel outwards along the radial direction. The presence of ripples is clear in images from $t = 13/500$ s onwards, although close inspection reveals their presence near the impingement point at $t = 3/500$ s. When the surface ripples reach a distance of about 4 cm from the rim, radial streaks originate and expand towards the edge of the sheet (figure 5*g*,*h*),

https://doi.org/10.1017/jfm.2015.137 Published online by Cambridge University Press

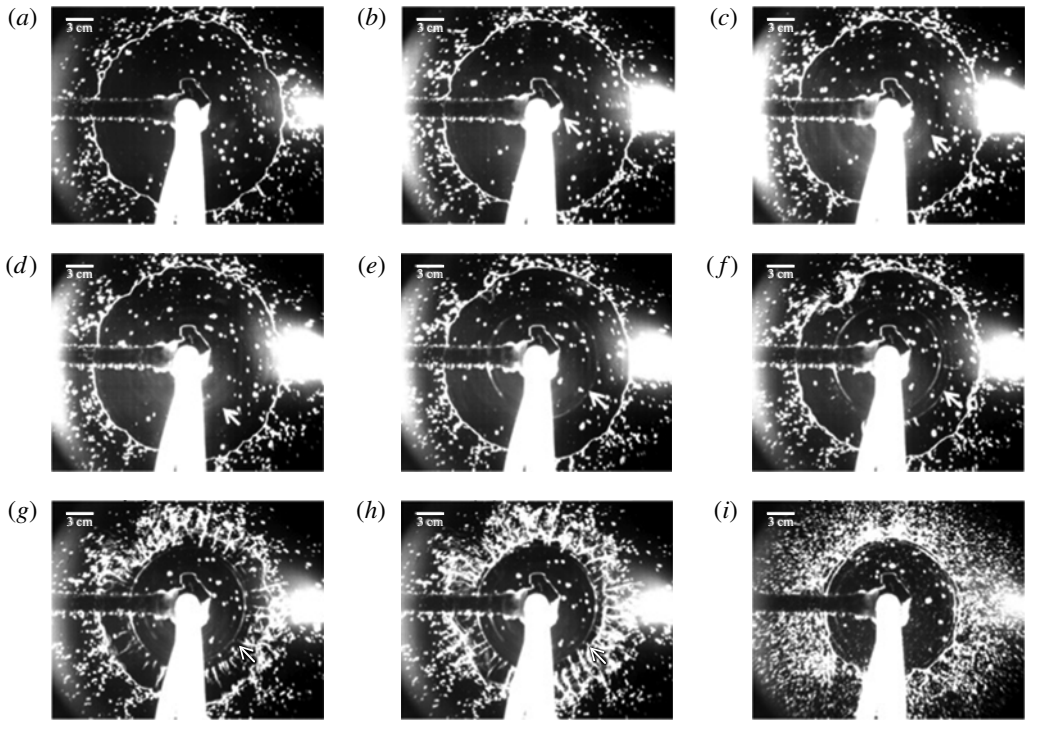


FIGURE 5. Time evolution of the deformation of a smooth liquid sheet ($We_d = 540$) excited by a disturbance introduced at the impingement point with a forcing frequency of 90 Hz and an SPL of 85 dB. The white scale bar at the top left corner of each image corresponds to 3.0 cm. The white arrow follows a sinuous wave as it moves out radially. The time elapsed after turning on the acoustics for each subfigure is as follows: (*a*) $t = 0$ s; (*b*) $t = 3/500$ s; (*c*) $t = 6/500$ s; (*d*) $t = 9/500$ s; (*e*) $t = 13/500$ s; (*f*) $t = 15/500$ s; (*g*) $t = 17/500$ s; (*h*) $t = 18/500$ s; (*i*) fully developed sheet.

leading to a catastrophic break-up of the sheet edge. The liquid sheet suddenly shrinks in size by ejecting tiny jets of water from the circumference of the sheet, as shown in figure 5(*g,h*). The liquid sheet finally reaches a stable but smaller size and continues to flap in response to the acoustics (figure 5*i*). These images appear similar to those of Mulmule *et al.* (2010), where the entire liquid sheet is subjected to external acoustic waves, and those of Bremond *et al.* (2007), where undulations were produced by a head-on impingement of a single laminar jet on a vibrating impactor.

As the above studies have demonstrated, the ripples correspond to sinuous waves that travel radially outwards from the impingement point. In the present case, the phase speed of the sinuous wave is smaller than the liquid speed, and this is confirmed by noting that the ripples (in figure 5) take about 0.034 s to travel about 7 cm radially outwards compared to 0.014 s (calculated from the known jet speed) for a liquid element for the same distance. The radius of the undisturbed sheet is about 10 cm (figure 5*a*). Furthermore, the time period of a single acoustic cycle in figure 5 is 0.011 s, indicating that every fluid element sees one full acoustic cycle before reaching the edge.

We used the LIF technique to capture the thickness modulations and thus the varicose mode of the undulating liquid sheet in the presence of acoustic forcing.

https://doi.org/10.1017/jfm.2015.137 Published online by Cambridge University Press

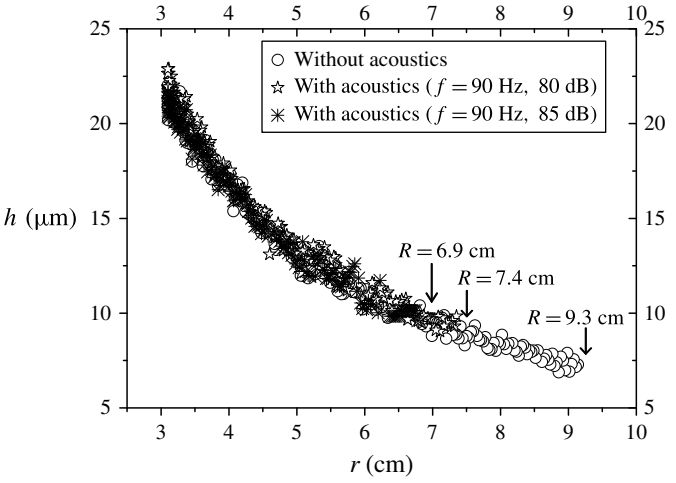


FIGURE 6. Thickness distribution of a fully developed liquid sheet ($We_d = 540$) when it is excited at 90 Hz at two different SPLs of 80 and 85 dB. Note that the thickness is plotted as a function of the radial distance from the impingement point. The distance between the fluorescent vertical section on the liquid sheet and the impingement location is 3.0 cm. The radial extent of the sheet (R) is included for each case.

Before performing the experiments on the liquid sheet, we tested the applicability of the technique on an undulating soap film forced by acoustics. The measured relative thickness distribution agreed well with those obtained via the interference technique (Boudaoud, Couder & Amar 1999) in terms of the location of the minima and maxima in the thickness distribution, thereby establishing the applicability of the LIF technique for measuring the thickness of undulating films.

Next, the thickness modulation was obtained for a liquid sheet at $We_d = 540$, subjected to a frequency of 90 Hz and forced at two different SPLs, namely, 80 and 85 dB. Capturing the initial transient in the thickness modulation, when the outer sections of the sheet break, was difficult because of the formation of radial streaks on the sheet. The latter appear as bright spots in the captured fluorescence images and prevent reliable measurement of the thickness during this time interval. Therefore, in all cases, measurements were made after the sheet had reached a stable size following the initial transient. The film thickness profile is presented in figure 6 for the two cases along with that measured in the absence of acoustics. As expected, the sheet radius R reduces with an increase in the SPL. Clearly, within the resolution of the technique (standard deviation of ± 0.5 μm), there are no perceptible thickness modulations in the liquid sheet at the two SPLs; they match with the thickness obtained in the absence of acoustics, indicating that thickness modulations, if any, are below the resolution of the experimental technique. Therefore, in what follows, the focus will be on the dynamics of the sinuous wave.

3.3. *Growth rates and phase velocities of the sinuous wave*

The centreline position of the liquid sheet was obtained by an analysis of images that were taken by the camera located at position 2 (figure 2*b*). The centreline position corresponds to the location of the maximum-intensity pixel along the length of the vertical fluorescent section of the liquid sheet. Experiments were performed in the

https://doi.org/10.1017/jfm.2015.137 Published online by Cambridge University Press

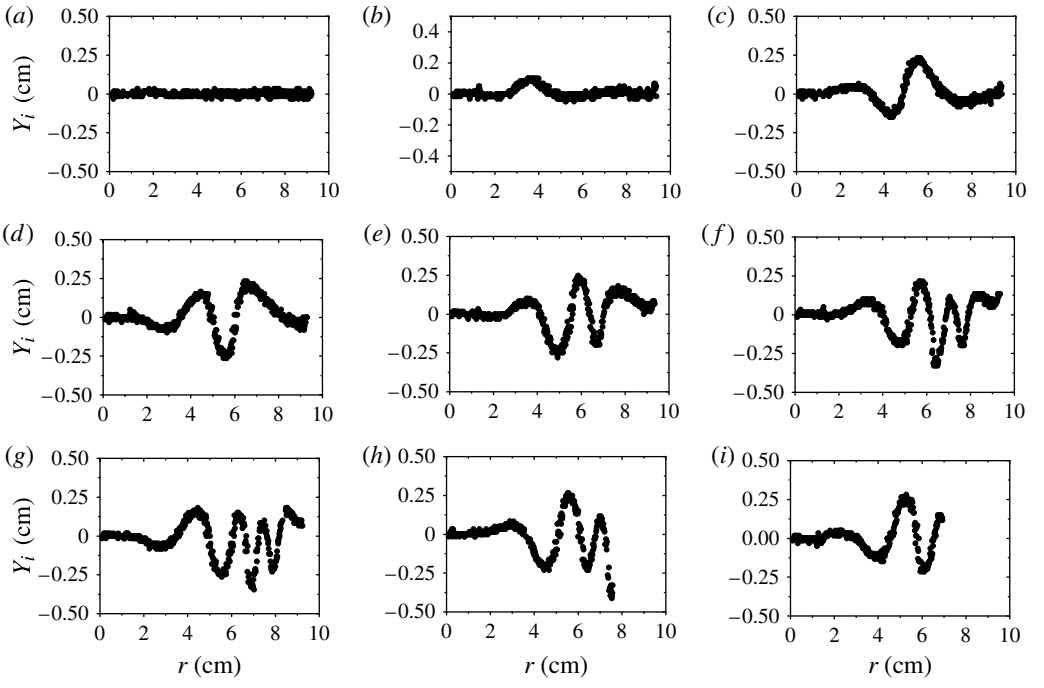


FIGURE 7. Time evolution of the sheet's centreline position for $We_d = 540$ when excited with a forcing frequency of 80 Hz and an SPL of 80 dB. The images are captured at a frame rate of 442 f.p.s. (*a*) $t = 0$ s; $R = 9.2$ cm, (*b*) $t = 3/442$ s; $R = 9.2$ cm, (*c*) $t = 7/442$ s; $R = 9.2$ cm, (*d*) $t = 10/442$ s; $R = 9.2$ cm, (*e*) $t = 14/442$ s; $R = 9.2$ cm, (*f*) $t = 19/442$ s; $R = 9.2$ cm, (*g*) $t = 21/442$ s; $R = 9.1$ cm, (*h*) $t = 24/442$ s; $R = 7.6$ cm, (*i*) $t = 27/442$ s; $R = 6.8$ cm. The radial position of the last point on the right gives the radial extent (R) of the sheet.

frequency range of 60–250 Hz and at different SPLs. Figure 7 presents the centreline position of the liquid sheet as a function of the radial coordinate at different time steps for $We_d = 540$ and for an acoustic forcing at 80 Hz, 80 dB. Here, Y_i is the deviation of the sheet's centreline position from its base state (i.e. in the absence of acoustics), and the time data in each subfigure correspond to the time elapsed after switching on the acoustics. The subfigure also includes the radius of the liquid sheet in each frame. The images for this data set were taken at a frame rate of 442 f.p.s.

As soon as the forcing is turned on, the central section of the liquid sheet is displaced first, which subsequently generates a sinuous wave that travels radially outwards. The amplitude of the wave increases initially as it propagates some distance, and thereafter starts to decrease close to the rim. The outer regions of the sheet break at around $t = 24/442$ s when the sinuous wave nearly reaches the rim of the sheet. Note that this occurs after more than four time cycles of forcing, confirming that regions close to the impingement point are displaced first. The sheet radius reduces to a stable value of 6.8 cm at $t = 27/442$ s, though the sheet continues to respond to forcing.

The time evolution of the sinuous wave yields the wave envelope that consists of data points corresponding to the maximum displacement of the sinuous wave along the length of the sheet. The envelope was obtained by overlapping the wave

https://doi.org/10.1017/jfm.2015.137 Published online by Cambridge University Press

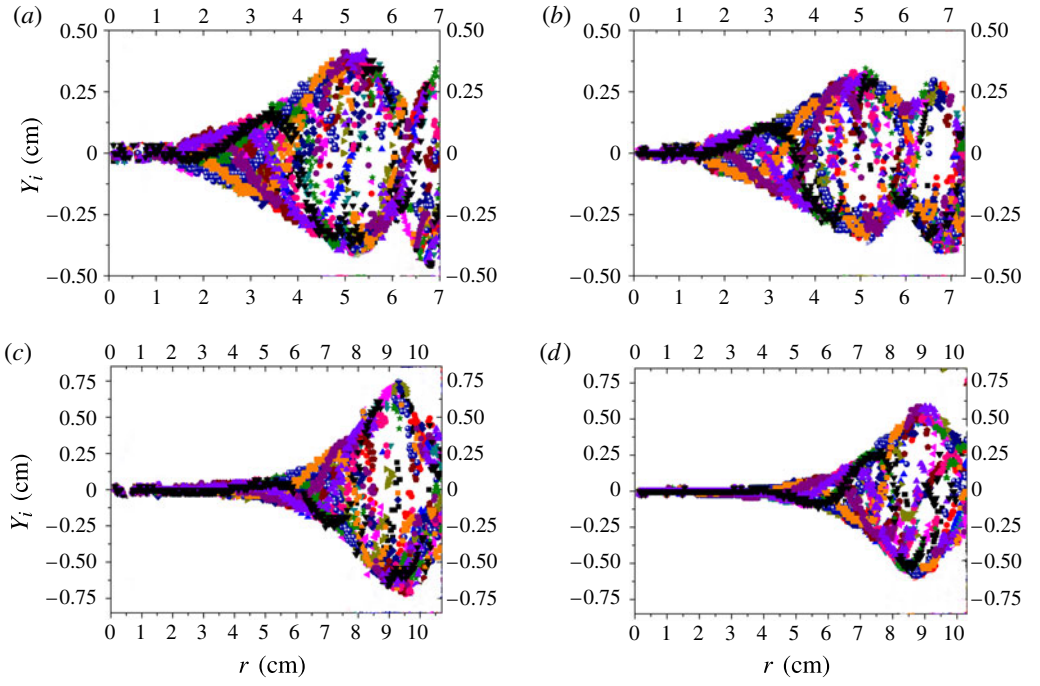


FIGURE 8. (Colour online) Experimental envelopes of a liquid sheet of $We_d = 540$ and 990 forced at frequencies of 80 and 90 Hz. (*a*) $We_d = 540$, 80 Hz, 85 dB; (*b*) $We_d = 540$, 90 Hz, 85 dB; (*c*) $We_d = 990$, 80 Hz, 70 dB; (*d*) $We_d = 990$, 90 Hz, 70 dB. In all four cases, the sheet has reached a steady size after an initial transient.

forms of at least 30 consecutive time points (more than four time cycles for most frequencies tested). Figure 8 presents four such plots, two each for $We_d = 540$ and 990. While the former corresponds to the smooth regime, the latter falls within the transition regime. Comparison of the overall profile of the envelopes indicates no qualitative difference between the profiles for the two regimes. In all four cases, the sheet-centreline displacement increases with radial location close to the impingement point, suggesting that the liquid sheet is spatially unstable to perturbations introduced close to the impingement point. The envelope exhibits a peak that occurs at a smaller radial distance for the lower We_d compared to that observed for $We_d = 990$. The envelope for the lower We_d appears to rise towards a second peak before reaching the edge of the sheet, while the sheet breaks before the appearance of such a feature at the higher We_d.

Given the similarity of the envelopes for the smooth and the transition regimes, in figures 9 and 10, we compare the measured envelope with the predictions of the recent theory of Tirumkudulu & Paramati (2013), which neglects the presence of the gas phase and is strictly applicable only in the smooth regime. The radial coordinate is rendered dimensionless with the diameter of the jet, $\tilde{r} \equiv r/d$, so that $\tilde{r}/(We_d/8) = 1$ corresponds to the edge of the circular sheet in the absence of acoustics (1.2). The non-dimensional displacements collapse for various SPLs in both cases, indicating a linear response. However, larger sheets are observed for lower SPLs. The breaking of the liquid sheet indicates the presence of thickness modulations. Bremond *et al.* (2007) suggest that a flapping sheet should be unstable to modulations induced by

https://doi.org/10.1017/jfm.2015.137 Published online by Cambridge University Press

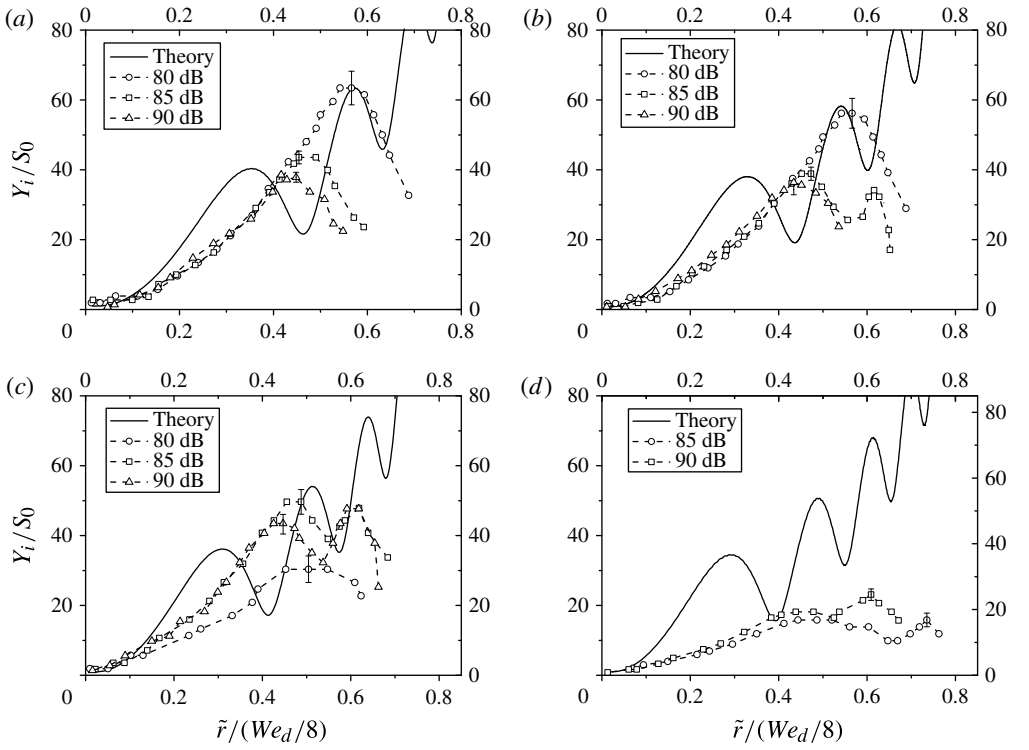


FIGURE 9. Sinuous wave envelope for $We_d = 540$ at varying forcing frequencies and SPLs. (*a*) 80 Hz; (*b*) 90 Hz; (*c*) 100 Hz; (*d*) 110 Hz.

Rayleigh–Taylor instability for large transverse oscillations of the liquid sheet. In our experiments, large initial amplitudes (due to high dB) for a fixed frequency would lead to large transverse acceleration downstream of the impingement point, thereby breaking the sheet at a lower radial distance. Such effects may be explained by accounting for the aforementioned instability, but are beyond the scope of the current investigations.

The experimental error in the measurement of the centreline position due to the finite size of the camera pixel is represented by an error bar, and is included only for the data point representing the maximum displacement. Note that the error bars for the rest of the data points for a given set have not been shown but are identical to those for the maximum displacement. The evolution of sinuous disturbance from theory is obtained by plotting the complex roots $(S_r(\bar{r})\cos(\bar{\omega}\bar{t}) - S_i(\bar{r})\sin(\bar{\omega}\bar{t}))$ of (1.8) at different time steps, where S_r and S_i are the real and imaginary parts, respectively, of the disturbance. The theoretical envelope was obtained by overlapping the above solution for many time steps for the experimental frequencies. The initial dimensionless displacement was obtained from the measured value closest to the impingement point. Figure 9 presents the results for the smooth regime ($We_d = 540$) for four different frequencies. At the lowest two frequencies, the predicted envelope exhibits a spatial growth rate similar to that observed, except for the presence of an early peak (or antinode) in the theoretical profile that is absent in the experiments. The magnitude of the envelopes predicted by theory matches remarkably well for distances far from the point of impingement (i.e. after the first peak). As the frequency

https://doi.org/10.1017/jfm.2015.137 Published online by Cambridge University Press

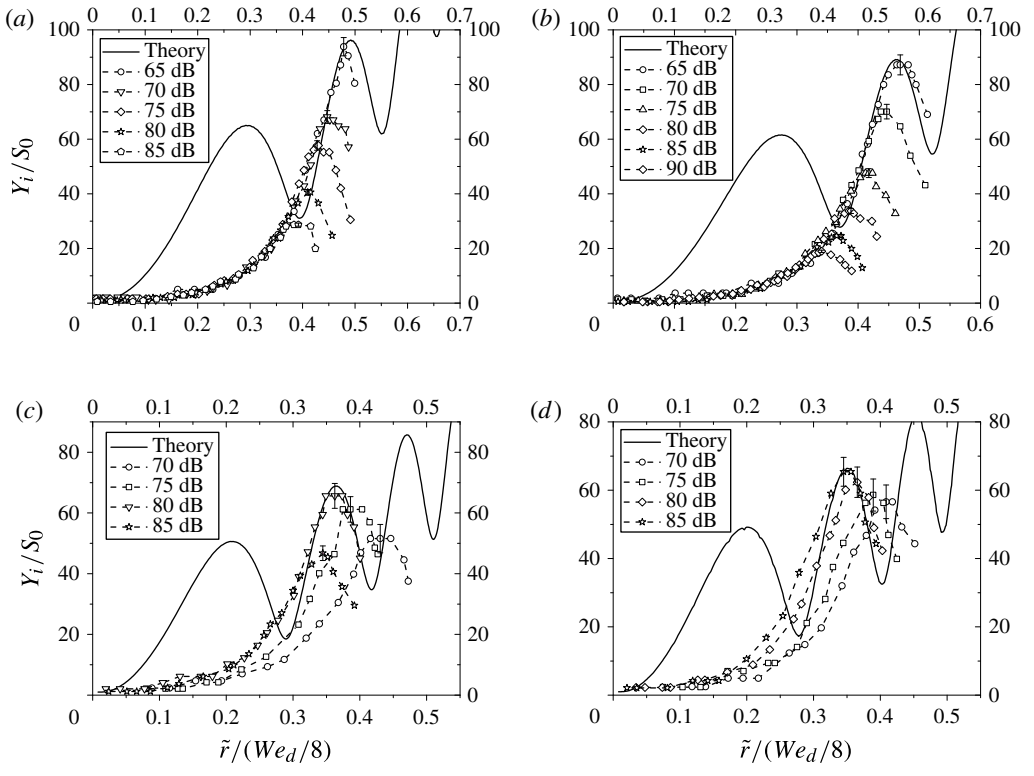


FIGURE 10. Sinuous wave envelope for $We_d = 990$ at varying forcing frequencies and SPLs. (*a*) 80 Hz; (*b*) 90 Hz; (*c*) 140 Hz; (*d*) 150 Hz.

increases, the theory predicts an increasing number of peaks in the envelope over the same spatial domain. A similar observation is made in experiments, where a second peak is observed at 100 Hz (85 and 90 dB). At the highest frequency tested (110 Hz), the measured envelope is below that predicted by theory. It was observed that as the frequency was increased, a larger SPL was required to observe a perceptible response. Thus a weak response was observed for 100 Hz at 80 dB, while there was no measurable response for 110 Hz at the same SPL. These observations can be explained by balancing the periodic forcing across a section of the liquid sheet close to the point of impingement with mass times the acceleration imparted to that section,

$$P_m \cos(\omega t) \sim h\rho_l \frac{\mathrm{d}^2 z}{\mathrm{d}t^2}, \tag{3.1}$$

where P_m is the magnitude of the pressure difference across the section of the sheet of thickness h, and z denotes the displacement of the section of the sheet. Integrating the above relation in time gives

$$z \sim \frac{P_m \cos(\omega t)}{h\rho_l \omega^2}, \tag{3.2}$$

suggesting that the displacement imparted to the impingement point will decrease inversely with the square of the forcing frequency. For small displacements, viscous

https://doi.org/10.1017/jfm.2015.137 Published online by Cambridge University Press

dissipation may damp out the disturbances, leading to non-overlapping growth curves (figure 9*c*).

Next, the predictions are compared to the envelopes obtained for the higher We_d (figure 10) which lies in the transition regime. As before, the measured envelopes collapse for the various SPLs for the two lower frequencies. In contrast to the lower We_d, only a single peak is observed at all frequencies and SPLs. The sheet was far more sensitive to perturbations, since an SPL as low as 65 dB was able to elicit a measurable response. Again, the first peak predicted by theory is missing in the experiments, although the observed trend of the sinuous disturbance is similar to that predicted and the height of the predicted envelope matches the measurements far from the impingement point. The sheet was unstable for a range of SPLs and for the frequencies tested. At the two higher frequencies of 140 and 150 Hz, the envelopes are similar only at the highest SPLs. These results clearly show that even at a Weber number as high as 990, the amplitude of the envelope predicted by the model is of the same magnitude as that observed in experiments. The mismatch between prediction and measurements for both high and low We_d occurs at short distances from the impingement point. Specifically, the first peak in the envelope is not observed in the experiments. While the cause of this discrepancy is not clear, it could be attributed to one of the several approximations made in the model. First, the model assumes that the sheet thickness is small compared to the radial distance; hence it is not applicable to regions close to the impingement point. As Crapper & Dombrowski (1984) note, the rapid rate of thinning in these regions would indeed influence the growth rate, and it is expected to be different from that predicted by our asymptotic solution. It is also possible that the presence of the surrounding gas phase in the experiments influences the initial growth rate due to the added mass effect, since for high initial growth rates the sheet will have to move the surrounding gas very rapidly, thereby increasing the inertia of the liquid sheet. Finally, the observed growth rates could also be lower due to the dampening effect of liquid and/or gas viscosity. Despite the approximations of the model, it should be noted that it is free of adjustable constants, and the envelope (non-dimensional) is a function of the Weber number and the forcing frequency alone.

At this stage, it is instructive to determine the stability of the liquid sheet in the presence of the gas phase from the analysis of Squire (1953), which accounts for the aerodynamic interactions in a constant-thickness sheet, and compare it with our theory. The dispersion equation of Squire obtained for a moving liquid sheet of constant thickness is given by

$$\rho_l \left(\frac{\omega}{k} - U\right)^2 \tanh\left(\frac{kh}{2}\right) + \rho_g \left(\frac{\omega}{k}\right)^2 = \sigma k, \tag{3.3}$$

where k is the wavenumber and the disturbance is assumed to be of the form $\exp(\mathrm{i}(kx - \omega t))$, where x is the spatial coordinate. In the limit of large wavelengths such that $kh \ll 1$, the dimensionless form of the dispersion relation reduces to

$$\tilde{k}^3 \left[\frac{1}{2} - \frac{4\tilde{r}}{We_d}\right] - \tilde{k}^2\tilde{\omega} + \tilde{k}\left[\frac{\tilde{\omega}^2}{2}\right] + 4\tilde{r}\delta\tilde{\omega}^2 = 0, \tag{3.4}$$

where $\delta = \rho_g/\rho_l$, $\tilde{k} = kd$, $\tilde{r} = r/d$, and $\tilde{\omega} = \omega d/U$ and the film thickness is a function of the radial coordinate ($h = d^2/4r$). It can be confirmed that in the absence of the gas phase ($\delta = 0$), the above equations predict temporal (neutral) stability irrespective

https://doi.org/10.1017/jfm.2015.137 Published online by Cambridge University Press

of the value of the film thickness. A similar, 'locally parallel' *ad hoc* assumption, applied to the stability (1.5) for sinuous disturbances on a radially expanding sheet with disturbance of the form $\exp(\mathrm{i}(kr-\omega t))$, gives an approximate dispersion relation that accounts for the effects of sheet thinning alone,

$$\tilde{k}^2\left[\frac{1}{2}-\frac{4\tilde{r}}{We_d}\right]+\tilde{k}\left[-\tilde{\omega}+\frac{\mathrm{i}}{\tilde{r}}\left(\frac{1}{2}+\frac{4\tilde{r}}{We_d}\right)\right]+\left[\frac{\tilde{\omega}^2}{2}-\mathrm{i}\frac{\tilde{\omega}}{2\tilde{r}}\right]=0, \tag{3.5}$$

where $\tilde{r}=r/d$. Close inspection of the above dispersion relation shows that it reduces to (3.4) for the case $\delta=0$, when $1/\tilde{r}\to 0$ ($4\tilde{r}/We_d$ is bounded).

For the experiments discussed here, wherein the forcing frequency is held fixed while the spatial growth of the sinuous wave is sought, we next investigate the spatial stability using the above two equations (3.4) and (3.5) to evaluate the relative importance of aerodynamic interactions and thinning on the stability of radially expanding liquid sheets. This involves treating $\tilde{k}$ as complex for given real values of $\tilde{\omega}$ and determining the wavenumber with the largest (in magnitude) negative imaginary part. Furthermore, it is confirmed that the solution satisfies the causality condition in that the corresponding group velocity is positive for $\tilde{x}, \tilde{r}>0$.

Figure 11 plots the most unstable spatial growth rate as a function of the radial distance obtained by solving (3.4), which accounts for aerodynamic interactions, and (3.5), which includes the effect of sheet thinning. For regions close to the impingement point and the rim, the spatial growth rates diverge due to the thinning effect. This is because of the imaginary terms in the coefficient of $\tilde{k}$. In comparison, the spatial growth rate due to the aerodynamic interactions increases from zero, reaching a maximum at some radial location and subsequently decreasing to zero within the extent of the radial sheet. For the low We_d (=540), the thinning effects dominate everywhere except for a small region where the spatial growth rates due to the aerodynamic effects are marginally greater. For the higher We_d, the aerodynamic effects dominate between radial positions (non-dimensional) of 0.1 and 0.65 while the thinning effects are important outside this region. These results suggest that while aerodynamic interactions will dominate at high We_d over the majority of the sheet, there will be regions close to the impingement point and near the sheet edge where thinning effects will dominate.

It is possible to determine the range of frequencies over which the most unstable spatial mode due to aerodynamic interactions is higher than that due to thinning for some radial location, so that for frequencies outside this range, the thinning effects dominate everywhere on the sheet (i.e. the dashed line in figure 11 is always below the solid line). Figure 12(*a*) presents the regime map obtained from such a calculation, which delineates regions where the thinning effects dominate from regions where both effects become important. The regime map applies for liquid sheets produced by the impingement of two jets. For $We_d<509$ and irrespective of the forcing frequency, the spatial growth rates due to the thinning effect are greater than those due to aerodynamic interactions at all radial locations of the thinning sheet. For $We_d>509$ and over a frequency range, the spatial growth rates due to aerodynamic effects are higher than those due to the thinning effect over a section of the sheet, though the predicted rates due to thinning diverge close to the impingement point and sheet edge, and always dominate at these locations. Thus $We_d=509$ is the critical Weber number above which the aerodynamic effects will become important over some section of the sheet and for a certain range of forcing frequencies. The plot includes our experimental points for both $We_d=540$ and 990 and at all forcing frequencies tested

https://doi.org/10.1017/jfm.2015.137 Published online by Cambridge University Press

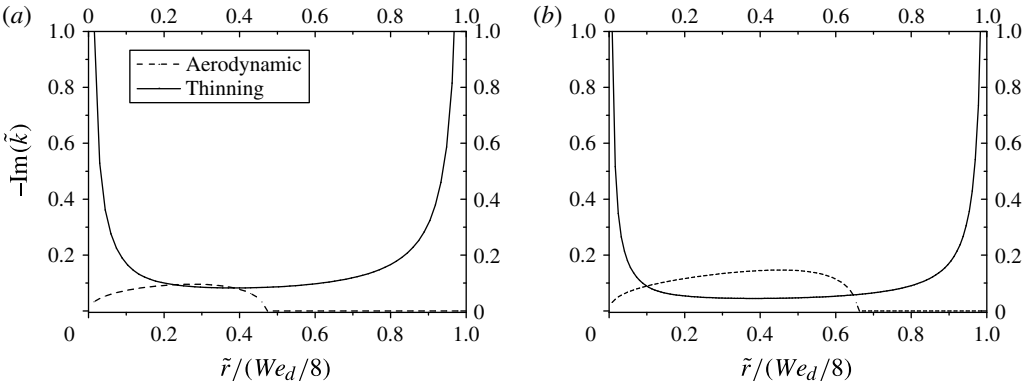


FIGURE 11. The most unstable spatial growth rate for the dispersion relation obtained from our theory (thinning) and that obtained from Squire's theory (aerodynamic) as a function of the radial location for $We_d = 540$ and 990 at 80 Hz. (*a*) $We_d = 540$, $\tilde{\omega} = 0.16$ (80 Hz); (*b*) $We_d = 990$, $\tilde{\omega} = 0.12$ (80 Hz).

in this study. Even though the points for $We_d = 540$ suggest an influence of both thinning and aerodynamic interactions, the plot of spatial growth rate versus radial position indicates that aerodynamic effects are marginally more important over a small region of the sheet while the thinning effects dominate everywhere else. However, at higher We_d, larger regions of the sheet are more susceptible to instabilities due to aerodynamic interactions than due to thinning effects. Yet, the nature of agreement between the predicted envelopes from our theory and those measured for both high and low We_d appears similar (figures 9 and 10). Indeed, Dombrowski and co-workers (Clark, Dombrowski & Pyott 1975) measured the spatial growth of sinuous waves on radially thinning liquid sheets produced by vibrating fan spray nozzles in the flapping regime, and found that Squire's analysis overpredicts the spatial growth rates for sinuous disturbances; they attributed the difference to the formation of vortices from wave crests, which dampen the wave growth.

More recently, Bremond *et al.* (2007) studied the dynamics of sinuous disturbances on a circular liquid sheet formed by a single laminar jet impinging on a vibrating impactor, and studied the growing sinuous wave in the transition/flapping regime. They derive the spatial growth rate from Squire's analysis (their (3.23)), based on which, they further derive an expression for a cut-off forcing frequency beyond which the sheet is unstable for radial distances less than the radius of the impact cylinder and thus considered stable. They find that the sinuous waves grow even for frequencies beyond the cut-off value and attribute it to the naturally most-amplified mode. The predicted growth rate from Squire's theory was found to be about twice that observed, and so they multiply the predicted growth rate by a factor of one half to match the measurements. However, in light of our findings, the sheet should be unstable even beyond the cut-off frequency, due to thinning effects where the spatial growth corresponding to the forcing frequency is determined from (1.8). For the case of a single jet impinging on an impactor, the film thickness is given by $h = d^2/8r$, and the corresponding dispersion relation that accounts for aerodynamic interactions is given by

$$\tilde{k}^3\left[\frac{1}{2} - \frac{8\tilde{r}}{We_d}\right] - \tilde{k}^2\tilde{\omega} + \tilde{k}\left[\frac{\tilde{\omega}^2}{2}\right] + 8\tilde{r}\delta\tilde{\omega}^2 = 0, \tag{3.6}$$

https://doi.org/10.1017/jfm.2015.137 Published online by Cambridge University Press

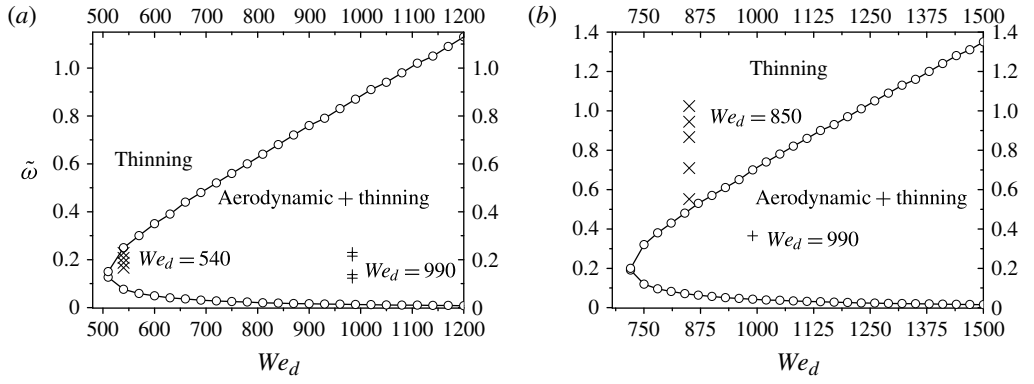


FIGURE 12. Regime map where the line (with ∘) delineates regions in the $\tilde{\omega}$–We_d space where the thinning effects dominate and regions where effects due to both aerodynamic interactions and thinning are important. (*a*) This plot corresponds to the case of the circular sheet produced by head-on impingement of two jets, where $h = d^2/4r$. The points $(\times, +)$ correspond to our experiments, $We_d = 540$ and 990. (*b*) This plot corresponds to the case of the circular sheet produced by a single jet impinging head-on onto an impactor, where $h = d^2/8r$. The points $(\times, +)$ correspond to experiments of Bremond *et al.* (2007) for $We_d = 850$ and 990.

while the dispersion relation due to thinning alone is

$$\tilde{k}^2\left[\frac{1}{2} - \frac{8\tilde{r}}{We_d}\right] + \tilde{k}\left[-\tilde{\omega} + \frac{\mathrm{i}}{\tilde{r}}\left(\frac{1}{2} + \frac{8\tilde{r}}{We_d}\right)\right] + \left[\frac{\tilde{\omega}^2}{2} - \mathrm{i}\frac{\tilde{\omega}}{2\tilde{r}}\right] = 0. \tag{3.7}$$

Note that (3.6) is identical to (3.23) of Bremond *et al.* (2007).

Figure 12(*b*) presents the regime map for liquid sheets produced by impingement of a single jet against an impactor and applies to the experiments of Bremond *et al.* (2007). In this case, the thinning effects dominate for $We_d < 721$ irrespective of the forcing frequency. Note that the critical value of $We_d = 721$ is $\sqrt{2}$ times that for the two-jet case and is a consequence of the different thickness-dependence on the radial distance. The plot also includes points for their experiments at $We_d = 850$ (140 to 260 Hz) and $We_d = 990$ (100 Hz). All frequencies for the lower We_d lie in the region where thinning dominates the spatial growth at all radial locations, and this is confirmed by plotting the most unstable spatial mode as a function of the radial distance for forcing frequencies of 240 Hz (figure 13*a*) and 140 Hz (figure 13*b*). While the spatial growth rates for thinning do not change much in this frequency range, those obtained from Squire's dispersion relation reduce in magnitude and radial extent with increasing frequency. At the highest frequency (260 Hz), the magnitude and radial extent of spatial modes from Squire's dispersion equation are insignificant compared to that obtained from our theory.

Figures 13(*c*) and 13(*d*) plot, respectively, the corresponding measured envelopes of Bremond *et al.* (2007) for the reported range of forcing frequencies for $We_d = 850$. Based on Squire's analysis, Bremond *et al.* (2007) predicted the sheet to be spatially stable for distances larger than the impactor's radius for frequencies larger than a cut-off frequency, which was determined as 220 Hz for $We_d = 850$. This is evident from figure 13(*a*) for 240 Hz, where the spatial growth due to aerodynamic interactions is confined to a small region close to the origin. Frequencies larger

https://doi.org/10.1017/jfm.2015.137 Published online by Cambridge University Press

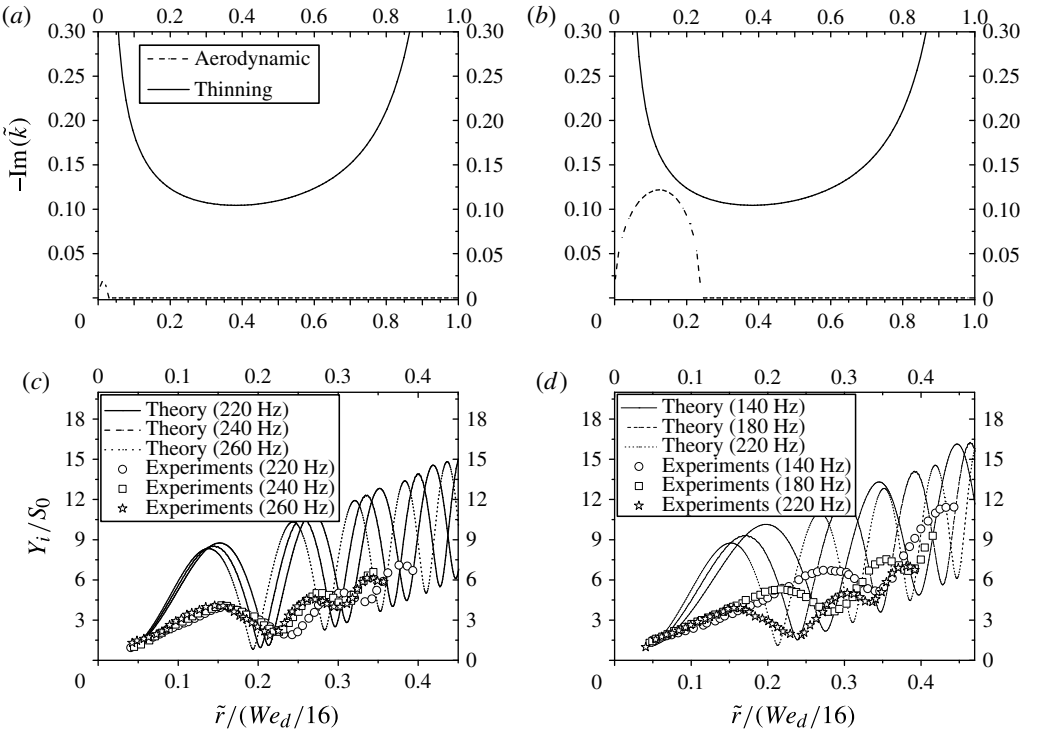


FIGURE 13. (*a*,*b*) The most unstable spatial growth rate for the dispersion relation obtained from our theory (thinning) and that obtained from Squire (aerodynamic) as a function of the radial location for $We_d = 850$, (*a*) 240 Hz, and (*b*) 140 Hz. (*c*,*d*) The measured sinuous wave envelope for $We_d = 850$ along with that predicted by (1.8) for (*c*) 220, 240 and 260 Hz, and (*d*) 140, 180, and 220 Hz. These conditions correspond to the experiments of Bremond *et al.* (2007). (*a*) $\tilde{\omega} = 0.95$ (240 Hz); (*b*) $\tilde{\omega} = 0.55$ (140 Hz); (*c*) $\tilde{\omega} = 0.55$ (140 Hz)–0.87 (220 Hz); (*d*) $\tilde{\omega} = 0.87$ (140 Hz)–1.02 (260 Hz).

than the cut-off value were considered to be in the stable forcing regime, while those below the value were supposed to be in the unstable forcing regime. Figures 13(*c*) and 13(*d*) also include the envelopes predicted by our theory. Here, the prediction of the sinuous wave envelope for the single-jet case is obtained by replacing the thickness profile for the two-jet case in (1.8) with that for a single jet, $h = d^2/8r$. While the differences between the amplitudes of the nodes and antinodes of the predicted envelopes are larger than those observed in the experiments and the locations of the nodes and antinodes appear to be somewhat shifted, the overall growth is close to the observations. Specifically, the predicted positions of the nodes (and antinodes) grow spatially at rates similar to those observed. Not only is the measured distance between the first and second node (or antinode) for each frequency close to the predicted value, the shift in the location of the nodes (and antinodes) to lower radial location with frequency is also captured correctly by our model. Finally, the predicted first antinodes for the three frequencies corresponding to the stable forcing regime (figure 13*c*) are very close together, while the distance is much larger for the lower frequencies (figure 13*d*) which belong to the unstable forcing regime. The proximity of the antinodes in the stable forcing regime was used as evidence to support their assumption that the naturally most-amplified mode will be dominant, irrespective

https://doi.org/10.1017/jfm.2015.137 Published online by Cambridge University Press

of the forcing frequency in the stable forcing regime. These features of the wave growth emerge naturally from our analysis which accounts for thinning of the sheet, suggesting that thinning effects play a dominant role here and are responsible for growth at all frequencies under these conditions.

While the above discussion has focused on the growth of disturbances, it is also important to compare the measured phase velocity of the disturbance with that predicted by the two theories. The phase velocity, in our experiments, was measured by tracking the position of a particular crest of the growing sinuous wave in successive frames. Theoretically, the dimensionless phase speed for the fastest growing spatial mode is given by

$$\tilde{v}_p = \frac{\tilde{\omega}}{\mathrm{Re}[\tilde{k}]}, \tag{3.8}$$

where $\mathrm{Re}[\tilde{k}]$ corresponds to the real part of the fastest growing spatial mode obtained from (3.4) and (3.5). Figure 14 compares the measured phase velocities for the two We_d and for the two frequencies from our experiments with those obtained from both (3.4) and (3.5). Recall that the spatial growth due to aerodynamic interactions spans only part of the sheet, which is reflected in the prediction for the corresponding phase speed for only that section of the sheet. The measured phase speeds of the spatially growing wave match remarkably well with the predictions that account for the thinning effect, while those due to the aerodynamic interactions are higher than the observed values. While these results are consistent with the trend observed for the spatial growth predicted by (3.5) for the lower We_d, the agreement for the case of higher We_d where aerodynamic interactions dominate over the measured radial positions is surprising. The latter results seem to suggest that even when aerodynamic interactions are dominant, the phase speed of the growing waves is governed by the thinning of the liquid sheet. A combined theory that accounts for both effects may help resolve this discrepancy observed at high We_d.

4. Conclusions

Radially expanding liquid sheets are produced by a head-on impingement of two laminar liquid jets. In this study, the thickness of the liquid sheet was measured using LIF, which agreed with the theoretical prediction obtained by a simple mass balance. When the impingement point is disturbed, sinuous waves produced close to the impingement point travel radially outwards. The phase speed of the sinuous waves decreases while their amplitude grows as they propagate radially outwards. Since there is no mechanism for energy dissipation in an inviscid liquid sheet and therefore the energy carried by the wave remains constant, the reducing wave speed and the thinning of the sheet causes the amplitude of the wave to increase in the radially outward direction. At the edge of the sheet the wave speed goes to zero, and so the amplitude diverges. Our experimental technique was unable to detect thickness variations when exposed to acoustic forcing, suggesting that the amplitude of the varicose modes was below the resolution of our experimental technique.

The phase speed and the envelope of the growing sinuous wave were compared with predictions of a recent theory for a radially expanding liquid sheet that accounts for liquid inertia, interfacial tension and thinning of the liquid sheet, while ignoring viscous effects and inertia of the surrounding gas. While the overall trend of the measured spatial growth of sinuous wave envelope for both $We_d = 540$ and 990 agreed with the theoretical predictions for radial locations far from the impingement point,

https://doi.org/10.1017/jfm.2015.137 Published online by Cambridge University Press

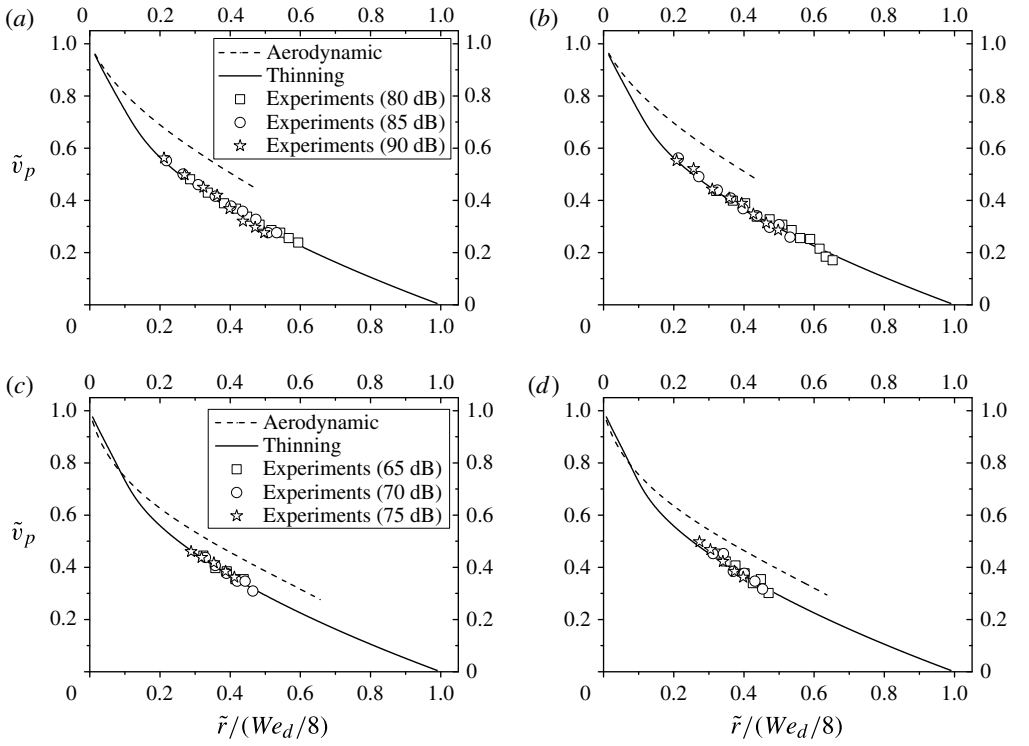


FIGURE 14. Measured sinuous-wave phase speed for $We_d = 540$ and 990 at varying forcing frequencies and SPLs along with predictions from (3.4) (aerodynamic) and (3.5) (thinning). (*a*) $We_d = 540$, $\tilde{\omega} = 0.16$ (80 Hz); (*b*) $We_d = 540$, $\tilde{\omega} = 0.19$ (90 Hz); (*c*) $We_d = 990$, $\tilde{\omega} = 0.12$ (80 Hz); (*d*) $We_d = 990$, $\tilde{\omega} = 0.14$ (90 Hz).

discrepancies were observed close to the impingement point. These disagreements are most likely due to the non-applicability of the asymptotic theory (which requires $h/r \ll 1$) close to the impingement point. However, there was remarkable agreement between the predicted phase speed and the measurements for both We_d and all forcing frequencies.

A comparison of the most unstable spatially growing wave mode obtained from the dispersion relation that accounts for thinning with that from Squire's analysis for a constant-thickness sheet that accounts for aerodynamic interactions shows that there exists a critical We_d below which thinning effects will dominate irrespective of the forcing frequency. For We_d greater than the critical value and over a frequency range, the spatial growth rates due to aerodynamic effects are higher than those due to the thinning effect over a section of the sheet – though the predicted rates due to thinning diverge close to the impingement point and sheet edge – and always dominate at these locations. Therefore, a correct theory for flows at high We_d would need to account for effects due to both thinning of the liquid sheet and interaction with the surrounding gas phase. More recently, Tammisola *et al.* (2011) have shown that the spatially growing sinuous waves in a constant-thickness liquid sheet is damped by the presence of viscous boundary layers near the liquid–gas interface, and thus the predicted spatial growth rate is lower than that predicted by Squire's analysis. A full theory would also need to account for such effects.

https://doi.org/10.1017/jfm.2015.137 Published online by Cambridge University Press

Before closing, it is important to note that one of the standard techniques in the stability literature is to make the 'locally parallel' assumption for systems where the geometry of the system changes slowly in the direction of disturbance propagation. What we show here is that such an approximation can be flawed if the full dynamics of the system is not properly accounted for.

Acknowledgements

The authors thank Professor S. J. Weinstein for comments on an earlier draft of this paper. The authors acknowledge the financial assistance from the Indo-French Center for Promotion of Advanced Research, a Swarnajayanti Fellowship of the Department of Science & Technology India, and the Indian Institute of Technology Bombay.

REFERENCES

ALEKSEENKO, S., ANTIPIN, V., CHERDANTSEV, A., KHARLAMOV, S. & MARKOVICH, D. 2009 Two-wave structure of liquid film and wave interrelation in annular gas liquid flow with and without entrainment. *Phys. Fluids* **21**, 1–5.

ASHGRIZ, N. (Ed.) 2011 *Handbook of Atomization and Sprays*, 1st edn. Springer.

BIRGE, R. R. 1987 *KODAK Laser Dyes*. Eastman Kodak Company.

BOUDAOUD, A., COUDER, Y. & AMAR, M. B. 1999 Self-adaptation in vibrating soap films. *Phys. Rev. Lett.* **82**, 3847–3850.

BREMOND, N., CLANET, C. & VILLERMAUX, E. 2007 Atomization of undulating liquid sheet. *Phys. Fluids* **585**, 421–456.

BROWN, R. C., ANDRUESSI, P. & ZANELLI, S. 1978 The use of wire probes for the measurement of liquid film thickness in annular gas–liquid flows. *J. Chem. Engng* **56**, 754–757.

CHOO, Y. J. & KANG, B. S. 2001 Parametric study on impinging jet liquid sheet thickness distribution using an interferometric method. *Exp. Fluids* **31**, 56–62.

CLARK, G. D., DOMBROWSKI, N. & PYOTT, G. A. D. 1975 Large amplitude Kelvin–Helmholtz waves on thin liquid sheets. *Proc. R. Soc. Lond.* A **342** (1629), 209–224.

CRAPPER, G. D. & DOMBROWSKI, N. 1984 A note on the effect of forced disturbances on the stability of thin liquid sheets and on the resulting drop size. *Intl J. Multiphase Flow* **10** (6), 731–736.

CRIMALDI, J. P. 2008 Planar laser induced fluorescence in aqueous flows. *Exp. Fluids* **44**, 851–863.

DOMBROWSKI, N., HASSON, D. & WARD, D. E. 1960 Some aspects of liquid flow through fan spray nozzles. *Chem. Engng Sci.* **12**, 35–50.

HIDROVO, H. C. & DOUGLAS, H. 2001 Emission and reabsorption of a laser induced fluorescence film thickness measurement. *Meas. Sci. Technol.* **12**, 467–477.

HUANG, J. C. P. 1970 The break-up of axisymmetric liquid sheets. *J. Fluid Mech.* **43**, 305–319.

LIANG, N. Y. & CHAN, C. K. 1997 Fast thickness profile measurement of a thin film by using a line scan charge coupled device camera. *Rev. Sci. Instrum.* **68**, 4525–4530.

LIN, S. P. & JIANG, W. Y. 2003 Absolute and convective instability of a radially expanding liquid sheet. *Phys. Fluids* **15**, 1745–1754.

MATSUMOTO, S. & TAKASHIMA, Y. 1971 Studies of the standard deviation of sprayed drop size distribution. *J. Chem. Engng Japan* **4** (3), 53–59.

MULMULE, A., TIRUMKUDULU, M. S. & RAMAMURTHI, K. 2010 Instability of a moving liquid sheet in the presence of acoustic forcing. *Phys. Fluids* **22**, 1–14.

SHEN, Y., MITTS, C. & POULIKAKOS, D. 1997 Holographic investigation of the effect of elevated ambient temperature on the atomization characteristics of impinging jet sprays. *Atomiz. Sprays* **7**, 123–142.

SQUIRE, H. B. 1953 Investigation of the instability of a moving liquid film. *Br. J. Appl. Phys.* **4**, 167–169.

https://doi.org/10.1017/jfm.2015.137 Published online by Cambridge University Press

TAMMISOLA, O., SASAKI, A., LUNDELL, F., MA, M. & SODERBERG, L. D. 2011 Stabilizing effect of surrounding gas flow on a plane liquid sheet. *J. Fluid Mech.* **672**, 5–32.

TAYLOR, G. I. 1959 The dynamics of thin sheets of fluid. Part II. Waves on fluid sheets. *Proc. R. Soc. Lond.* A **253**, 296–312.

TIRUMKUDULU, M. S. & PARAMATI, M. 2013 Stability of a moving radial liquid sheet: time-dependent equations. *Phys. Fluids* **25**, 102107.

VILLERMAUX, E. & CLANET, C. 2002 Life of flapping liquid sheet. *J. Fluid Mech.* **462**, 341–366.

WAKIMOTO, T. & AZUMA, T. 2004 Instability of radial liquid sheet flow. *Trans. JSME* **47**, 9–19.

WEIHS, D. 1978 Stability of thin, radially moving liquid sheets. *J. Fluid Mech.* **87**, 289–298.

https://doi.org/10.1017/jfm.2015.137 Published online by Cambridge University Press